


 Cite this: *RSC Adv.*, 2025, **15**, 33648

Synthesis of $\text{Li}_7\text{P}_3\text{S}_{11}$ solid electrolyte in ethyl propionate medium for all-solid-state Li-ion battery

 Tran Anh Tu^{abc} and Nguyen Huu Huy Phuc^{id *abc}

In this study, we report a facile wet chemical synthesis method for preparing $\text{Li}_7\text{P}_3\text{S}_{11}$ solid-state electrolyte using ethyl propionate as the solvent. The structures of the samples were investigated using X-ray diffraction, Raman spectroscopy, and ^{31}P nuclear magnetic resonance. The electrochemical properties of the samples were evaluated using cyclic voltammetry, direct current, and alternating-current electrochemical impedance measurements. The $\text{Li}_7\text{P}_3\text{S}_{11}$ solid electrolyte (SE) exhibited a Li^+ conductivity of $1.5 \times 10^{-3} \text{ S cm}^{-1}$ at 25°C . The electrochemical measurements confirmed that the synthesized electrolyte is a single Li^+ conductor with stability up to $5.0 \text{ V vs. Li}^+/\text{Li}$. Furthermore, a solid-state battery (SSB) cell incorporating $\text{LiNi}_{1/3}\text{Mn}_{1/3}\text{Co}_{1/3}\text{O}_2$ and the synthesized $\text{Li}_7\text{P}_3\text{S}_{11}$ maintained stability for up to 50 cycles, demonstrating the durability of $\text{Li}_7\text{P}_3\text{S}_{11}$ in high-voltage SSB applications. These results indicate that $\text{Li}_7\text{P}_3\text{S}_{11}$ SE is a promising candidate for rechargeable solid-state Li-ion batteries.

Received 22nd July 2025

Accepted 10th September 2025

DOI: 10.1039/d5ra05281e

rsc.li/rsc-advances

1. Introduction

Solid-state batteries (SSBs) are a class of batteries that use solid electrolytes (SEs) instead of the liquid or gel electrolytes employed in conventional lithium-ion batteries.¹ SSBs offer significant advantages over conventional batteries, including higher energy density and improved safety, making them a promising technology for future energy storage, particularly in electric vehicles. SSBs can store more energy within the same volume or weight than conventional batteries, enabling longer ranges for electric vehicles.² The use of SEs, which are more stable and less prone to leakage or fire than liquid electrolytes, significantly improves safety.

Sulfide solid electrolytes are considered as promising materials for SSBs because of their high ionic conductivity, mechanical flexibility, and high energy density.^{3,4} Among them, $\text{Li}_7\text{P}_3\text{S}_{11}$ SE has been extensively studied for its ionic conductivity ranging from 10^{-4} to $10^{-2} \text{ S cm}^{-1}$ at room temperature.⁵ $\text{Li}_7\text{P}_3\text{S}_{11}$ synthesized *via* solid-state reactions has achieved a maximum ionic conductivity of $1.7 \times 10^{-2} \text{ S cm}^{-1}$ at room temperature.⁶ However, solid-state reactions are energy-intensive, which limits their scalability for mass production. In contrast, liquid-phase synthesis offers a more versatile

approach for the scalable production and preparation of electrode composite materials for all SSBs.⁷

Liquid-phase synthesis of $\text{Li}_7\text{P}_3\text{S}_{11}$ has recently been reported, leveraging its compatibility with composite electrode preparation.^{8,9} Among the solvents used in $\text{Li}_7\text{P}_3\text{S}_{11}$, acetonitrile (ACN) is the most widely used, as it enables SEs with ionic conductivity up to $9.7 \times 10^{-4} \text{ S cm}^{-1}$ at 25°C .¹⁰ In CAN, Li_2S reacts with P_2S_5 to form Li_3PS_4 and $\text{Li}_4\text{P}_2\text{S}_7$ precipitates in a 1:1 molar ratio.¹¹ After solvent removal, the residues $\text{Li}_4\text{P}_2\text{S}_7 \cdot \text{ACN}$ and $\text{Li}_3\text{PS}_4 \cdot \text{CAN}$, yielded $\text{Li}_7\text{P}_3\text{S}_{11}$ upon heat treatment at elevated temperatures as ACN was removed. Recently, ethyl acetate (EA) was used to synthesize $\text{Li}_7\text{P}_3\text{S}_{11}$, yielding an ionic conductivity of $1.05 \times 10^{-3} \text{ S cm}^{-1}$ at 25°C .¹² Unlike in CAN, Li_2S and P_2S_5 completely dissolved in EA to form $\text{Li}_7\text{P}_3\text{S}_{11}$. Other solvents, such as 1,2-dimethoxyethane and tetrahydropyran, have also been used for the synthesis of $\text{Li}_7\text{P}_3\text{S}_{11}$ SE.^{13,14} Ethyl propionate (EP) has previously been used to synthesize $\beta\text{-Li}_3\text{PS}_4$, $\text{Li}_7\text{P}_2\text{S}_8\text{I}$, and Li_3PO_4 -doped Li_3PS_4 , but not $\text{Li}_7\text{P}_3\text{S}_{11}$.¹⁵⁻¹⁸

In this study, $\text{Li}_7\text{P}_3\text{S}_{11}$ SE was synthesized using EP to facilitate the reaction between Li_2S and P_2S_5 . Li_2S and P_2S_5 (70:30 molar ratio) did not fully dissolve in EP, resulting in the formation of a white precipitate and a yellowish solution. After solvent removal, the residue was heated at 250°C for 1 h to yield $\text{Li}_7\text{P}_3\text{S}_{11}$ SE. The prepared $\text{Li}_7\text{P}_3\text{S}_{11}$ SE exhibited an ionic conductivity of $1.5 \times 10^{-3} \text{ S cm}^{-1}$ at 25°C , comparable to previously reported values. A solid-state half-cell using Li_3InCl_6 -coated $\text{LiNi}_{1/3}\text{Mn}_{1/3}\text{Co}_{1/3}\text{O}_2$ as the active material and $\text{Li}_7\text{P}_3\text{S}_{11}$ demonstrated stable cycling performance, indicating the compatibility of the synthesized $\text{Li}_7\text{P}_3\text{S}_{11}$ SE with high-voltage materials.

^aFaculty of Materials Technology, Ho Chi Minh City University of Technology (HCMUT), 268 Ly Thuong Kiet Str., Dist. 10, Ho Chi Minh City, Vietnam. E-mail: nhphuc@hcmut.edu.vn

^bNational Key Laboratory of Polymer and Composite Materials, 268 Ly Thuong Kiet, District 10, Ho Chi Minh City, Vietnam

^cVietnam National University Ho Chi Minh City, Linh Trung Ward, Thu Duc Dist., Ho Chi Minh City, Vietnam



2. Experimental

2.1 Chemicals

Li_2S (99.9%, Macklin), P_2S_5 (99%, Macklin), LiCl (99.9%, Macklin), InCl_3 (99.99%, Macklin), and super-dehydrated EP (Aldrich) were used as received without further treatment.

2.2 Liquid-phase synthesis of $\text{Li}_7\text{P}_3\text{S}_{11}$

A mixture of 2.0 g of Li_2S and P_2S_5 (7 : 3 molar ratio) was weighed and placed in a three-necked flask with 40 ml of EP. The mixture was stirred at 300 rpm and 50 °C for 24 h, yielding a suspension containing a white precipitate and a yellowish solution (Fig. S1). The solvent was evaporated from the suspension under reduced pressure at room temperature to obtain a residue (S-RT). The residue was then ground using an agate mortar and heat-treated in an Ar atmosphere for 1 h at 190 °C (S-190), followed by 1 h at 230 °C, 240 °C and 250 °C to obtain $\text{Li}_7\text{P}_3\text{S}_{11}$ SE (denoted as S-230, S-240, and S-250, respectively).

2.3 Li_3InCl_6 -modified $\text{LiNi}_{1/3}\text{Mn}_{1/3}\text{Co}_{1/3}\text{O}_2$ preparation

Li_3InCl_6 -modified $\text{LiNi}_{1/3}\text{Mn}_{1/3}\text{Co}_{1/3}\text{O}_2$ (NMC111, MTI) containing 2 wt% Li_3InCl_6 was prepared following a reported procedure.¹⁹ Li_3InCl_6 was synthesized according to a previously reported method.²⁰ Li_3InCl_6 was dissolved in anhydrous ethanol to form a uniformly transparent solution, into which NCM111 powder was added. After solvent evaporation at 80 °C, the precursor powder was further sintered at 400 °C under a nitrogen atmosphere to yield the composite powder (LIC@NMC111).

2.4 Structural characterization

The structure and morphology of the prepared samples were characterized using thermogravimetry-differential thermal analysis (TG-DTA, EVO II, Rigaku), X-ray diffraction (XRD, X8, Bruker), Raman spectroscopy (Horiba LabRam HR spectrometer, 532 nm), solid-state ^{31}P nuclear magnetic resonance (^{31}P NMR, Avance III 400, Bruker), scanning electron microscopy (SEM, S4800, Hitachi), and energy-dispersive X-ray spectroscopy (EDS, ULTIM MAX, Oxford Instrument).

The samples were prepared in an Ar-filled glove box and loaded into an airtight sample holder for characterization.

2.5 Electrochemical measurements

The electrical conductivity of a pellet prepared by uniaxially cold-pressing ~200 mg of powder at 510 MPa was measured. Alternating-current impedance spectroscopy was performed using a potentiostat (PGSTAT302N, Autolab, Herisau, Switzerland) over a frequency range of 10 MHz–10 Hz.

DC conductivities were measured using blocking and non-blocking electrodes, in which stainless-steel rods and Li metal sheets were employed as the electrodes, respectively. The pelletized sample was prepared by cold-pressing S-250 powder at 510 MPa. For nonblocking electrodes, the Li metal sheets (~8 mm diameter, 0.1 mm thickness) were attached to both faces of the pellet at room temperature. A 0.5 V DC was applied

to the cells, and the current was measured using a potentiostat (SI 1287, Solatron) to determine the dominant mobile ions.

The electrochemical compatibility was tested using a $\text{Li}|\text{SE}|\text{Au}$ cell (Au sputtered on a stainless-steel rod) at a scan rate of 5 mV s⁻¹ between 0.5 and 5 V with a potentiostat (SI 1287, Solatron).

The SSB half-cell was fabricated using the following process. The cathode composite was prepared by manually mixing LIC@NMC111 and S-250 in a 70 : 30 weight ratio using an agate mortar. A bilayer pellet (10 mm diameter) consisting of the electrode composite (12 mg) and S-250 (100 mg) was obtained by cold-pressing at 310 MPa. Indium (99.99%, Macklin) and Li foil were attached to opposite sides of the SE. The cell was assembled by sandwiching the pellet between stainless-steel rods and cycled in the constant-current mode at 0.1C between 3.70 and 2.40 V vs. Li-In.

3. Results and discussion

Fig. 1a shows the TG-DTA curves of the S-RT. The TG curve shows two distinct stages of the mass loss process: Stage 1 occurs from approximately 50 °C to 160 °C, and Stage 2 from 270 °C to 290 °C. The DTA curve displays several endothermic peaks between 30 °C and 150 °C, along with two exothermic peaks in the ranges of 150–200 °C and 270–290 °C. The mass loss in Stage 1 is attributed to the removal of crystallized solvent molecules. The $\text{P}_2\text{S}_7^{4-}$ group in $\text{Li}_7\text{P}_3\text{S}_{11}$ is known to decompose at elevated temperatures, forming sulfur and $\text{P}_2\text{S}_6^{4-}$.²¹ Therefore, the exothermic peak and accompanying mass loss in Stage 2 (270–290 °C) are ascribed to the decomposition of the $\text{P}_2\text{S}_7^{4-}$ group in the sample. Fig. 1b shows the first-order derivatives of the TG and DTA curves. The first-order differential curves of TG-DTA show that the EP solvent removal process finishes at ~170 °C. The $d(\text{DTA})$ curve illustrates an endothermic phenomenon between 230 °C and 250 °C without any mass loss, indicating the formation of $\text{Li}_7\text{P}_3\text{S}_{11}$. Notably, another endothermic phenomenon started at ~250 °C, accompanied by mass loss, corresponding to the decomposition of $\text{P}_2\text{S}_7^{4-}$ ions to $\text{P}_2\text{S}_6^{4-}$. Based on these TG-DTA results, the experimental samples obtained after removal of the EP solvent at room temperature were heated at 190 °C for 1 h, followed by heat treatments at 230 °C, 240 °C, and 250 °C for 1 h to examine the formation of $\text{Li}_7\text{P}_3\text{S}_{11}$.

Fig. S2 shows the XRD patterns of the precipitate obtained after decanting the yellow supernatant (Fig. S1), along with Li_2S for comparison. The precipitate pattern shows no residual Li_2S , indicating complete consumption of Li_2S in the reaction with P_2S_5 in the EP medium under specific conditions. Notably, the precipitate pattern resembled that of the Li_3PS_4 precursor synthesized from Li_2S and P_2S_5 in the EP medium.¹⁵ Fig. 2 shows the XRD patterns of Li_2S , P_2S_5 , and the prepared samples. The Li_2S pattern exhibits peaks at $2\theta \approx 26^\circ$ and 31° , while P_2S_5 appears nearly amorphous to XRD. The residue pattern after solvent removal at room temperature (S-RT) shows many peaks that do not correspond to known crystal structures. The absence of Li_2S in the S-RT pattern indicates that Li_2S has completely reacted with P_2S_5 in the EP medium. The pattern of the sample



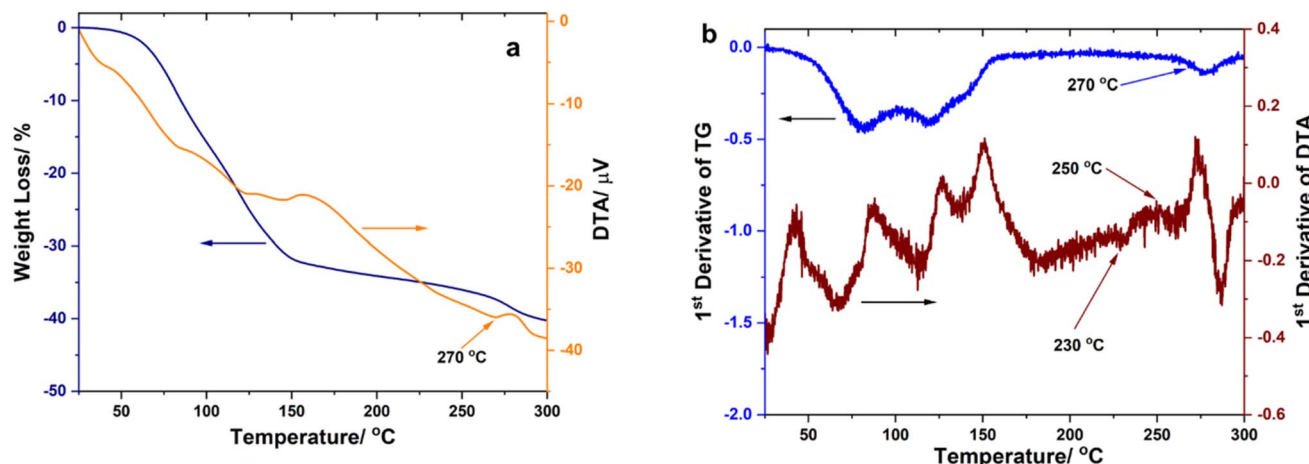


Fig. 1 (a) TG and DTA curves of S-RT; (b) TG and DTA first-order derivatives of S-RT.

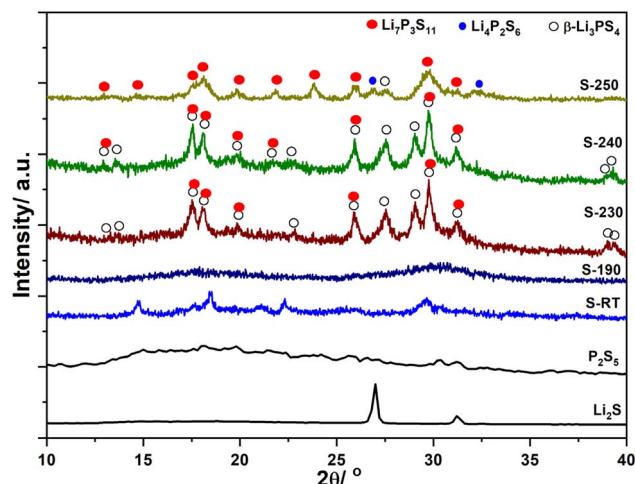


Fig. 2 XRD patterns of Li₂S, P₂S₅, and the prepared samples S-RT, S-190, S-230, S-240, and S-250.

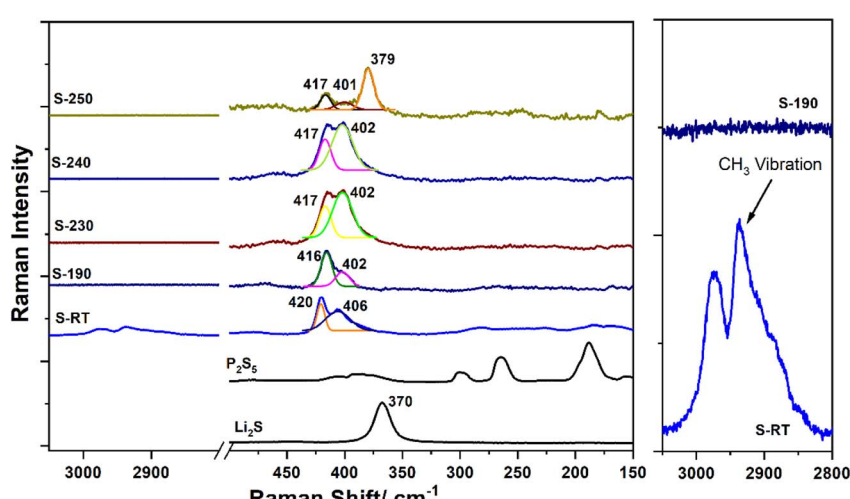


Fig. 3 Raman spectra of Li₂S, P₂S₅, and the prepared samples S-RT, S-190, S-230, S-240, and S-250. The figure on the right-hand side shows the enlargement in the range of 3050 to 2800 cm^{-1} of the spectra of S-RT and S-190.



consumption of Li_2S in the reaction with P_2S_5 . Fig. 3 shows the Raman spectra of Li_2S , P_2S_5 , and the prepared samples S-RT, S190, S-230, S-240, and S250. The inset on the left shows an enlarged view of the $3100\text{--}2800\text{ cm}^{-1}$ region for the S-RT and S-190 spectra. The Li_2S spectrum exhibited a single intense peak at 370 cm^{-1} , while the P_2S_5 spectrum exhibited multiple peaks between 150 and 320 cm^{-1} . The S-RT spectrum shows peaks at 406 , 420 , 2940 , and 2965 cm^{-1} , with no main peaks from Li_2S or P_2S_5 detected, indicating a complete reaction between Li_2S and P_2S_5 . This observation is consistent with the XRD results. The peaks at 2940 and 2965 cm^{-1} correspond to CH_3 group vibrations in EP.¹⁵ The peaks at 406 and 420 cm^{-1} are attributed to the local structure units of $\text{P}_2\text{S}_7^{4-}$ and PS_4^{3-} in $\text{Li}_4\text{P}_2\text{S}_7$ and Li_3PS_4 , respectively.²⁶ The S-190 spectrum exhibits peaks at 402 and 416 cm^{-1} , indicating the presence of $\text{P}_2\text{S}_7^{4-}$ and PS_4^{3-} in $\text{Li}_4\text{P}_2\text{S}_7$ and Li_3PS_4 , respectively. The absence of CH_3 vibration peaks indicates the effective removal of EP after heating at $190\text{ }^\circ\text{C}$ for 1 h . The positions of the PS_4^{3-} and $\text{P}_2\text{S}_7^{4-}$ peaks in S-190 were shifted relative to those in the S-RT sample, indicating strong interactions between Li_3PS_4 and $\text{Li}_4\text{P}_2\text{S}_7$ with the EP solvent molecules. This observation suggests that EP removal from S-RT resulted in the formation of an amorphous structure in S-190, which is consistent with the XRD results. The spectra of S-230 and S-240 show the presence of $\text{P}_2\text{S}_7^{4-}$ and PS_4^{3-} with peaks at 402 and 417 cm^{-1} , respectively. The spectrum of S-250 exhibits peaks at 417 , 401 , and 379 cm^{-1} , corresponding to the local structure units of PS_4^{3-} and $\text{P}_2\text{S}_7^{4-}$ in $\text{Li}_7\text{P}_3\text{S}_{11}$, and $\text{P}_2\text{S}_6^{4-}$ in $\text{Li}_4\text{P}_2\text{S}_6$, respectively.^{8,26,27} These Raman results confirm the

presence of $\text{Li}_7\text{P}_3\text{S}_{11}$ and $\text{Li}_4\text{P}_2\text{S}_6$ phases in S-250, which is consistent with the XRD measurements.

Powder XRD is effective for identifying crystalline phases but cannot characterize amorphous components. Therefore, ^{31}P NMR was employed as a complementary technique to investigate the local structure of samples S-240 and S-250 (Fig. 4a and b, respectively). The S-240 spectrum exhibited peaks at the characteristic positions of the PS_4^{3-} and $\text{P}_2\text{S}_7^{4-}$ groups in $\text{Li}_7\text{P}_3\text{S}_{11}$.²⁸⁻³⁰ The deconvolution result revealed peaks at 86.9 , 87.8 , 88.9 , and 91.7 ppm . The peak at 86.9 ppm corresponds to PS_4^{3-} unit in $\beta\text{-Li}_3\text{PS}_4$,³¹ while the peaks at 87.8 and 88.9 ppm are attributed to PS_4^{3-} and $\text{P}_2\text{S}_7^{4-}$ units in $\text{Li}_7\text{P}_3\text{S}_{11}$, respectively.²⁸⁻³⁰ The broad peak at 91.7 ppm is attributed to the $\text{P}_2\text{S}_7^{4-}$ group in amorphous $\text{Li}_4\text{P}_2\text{S}_7$,³² indicating the presence of $\beta\text{-Li}_3\text{PS}_4$, $\text{Li}_7\text{P}_3\text{S}_{11}$, and amorphous $\text{Li}_4\text{P}_2\text{S}_7$ in S-240. The S-250 spectrum exhibits peaks at the characteristic positions of the PS_4^{3-} and $\text{P}_2\text{S}_7^{4-}$ groups in $\text{Li}_7\text{P}_3\text{S}_{11}$ and $\text{P}_2\text{S}_6^{4-}$ in $\text{Li}_4\text{P}_2\text{S}_6$.²⁸⁻³⁰ The deconvolution result revealed peaks at 86.3 , 87.8 , 89.9 , 91.8 , 105.2 , and 108.7 ppm . The peak at 86.9 ppm corresponds to the PS_4^{3-} of the structural unit in $\beta\text{-Li}_3\text{PS}_4$.³¹ The peaks at 87.8 and 89.9 ppm are attributed to PS_4^{3-} and $\text{P}_2\text{S}_7^{4-}$ groups in $\text{Li}_7\text{P}_3\text{S}_{11}$, respectively, while the broad peak at 91.7 ppm arises from $\text{P}_2\text{S}_7^{4-}$ group in amorphous $\text{Li}_4\text{P}_2\text{S}_7$. Notably, the area ratio between the $\text{P}_2\text{S}_7^{4-}$ peak in amorphous $\text{Li}_4\text{P}_2\text{S}_7$ and $\text{Li}_7\text{P}_3\text{S}_{11}$ of S-250 is smaller than that of S-240, indicating the transformation of amorphous $\text{Li}_4\text{P}_2\text{S}_7$ into crystalline $\text{Li}_7\text{P}_3\text{S}_{11}$. The peaks at 105.2 and 108.7 ppm correspond to the $\text{P}_2\text{S}_6^{4-}$ structural unit in $\text{Li}_4\text{P}_2\text{S}_6$ (ref. 32-34). The formation of $\text{Li}_4\text{P}_2\text{S}_6$

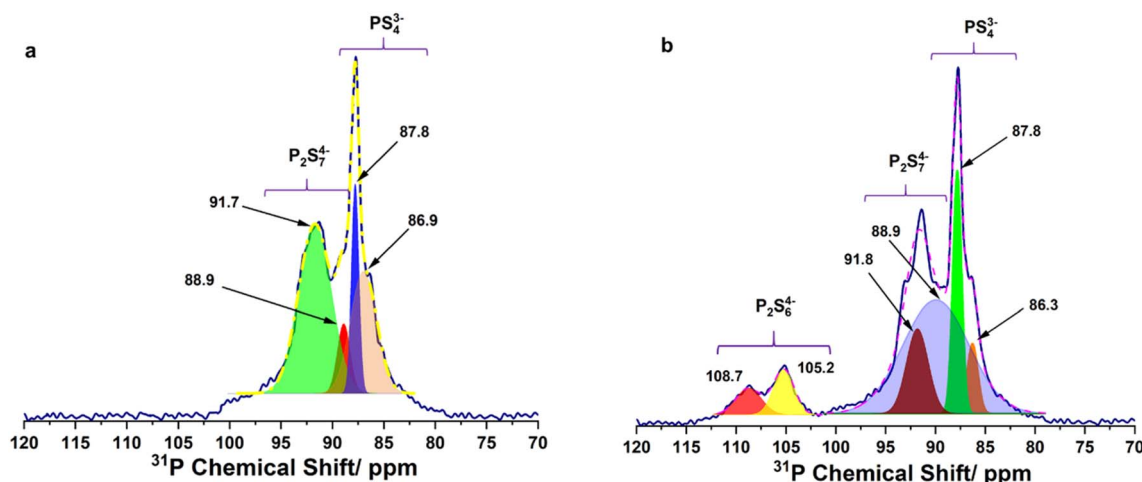


Fig. 4 ^{31}P NMR spectra of (a) S-240 and (b) S-250.

Table 1 Summary of the liquid-phase processing data of $\text{Li}_7\text{P}_3\text{S}_{11}$ solid electrolytes

Solvent	Ionic conductivity ($25\text{ }^\circ\text{C}$)/ S cm^{-1}	Processing temperature/ $^\circ\text{C}$	Activation energy E_a/eV	Electrochemical window/V vs. Li^+/Li	Reference
ACN	9.7×10^{-4}	250	0.323	5.0	10
EA	1.05×10^{-3}	260	—	—	12
EP	1.5×10^{-3}	250	0.27	5.0	This work



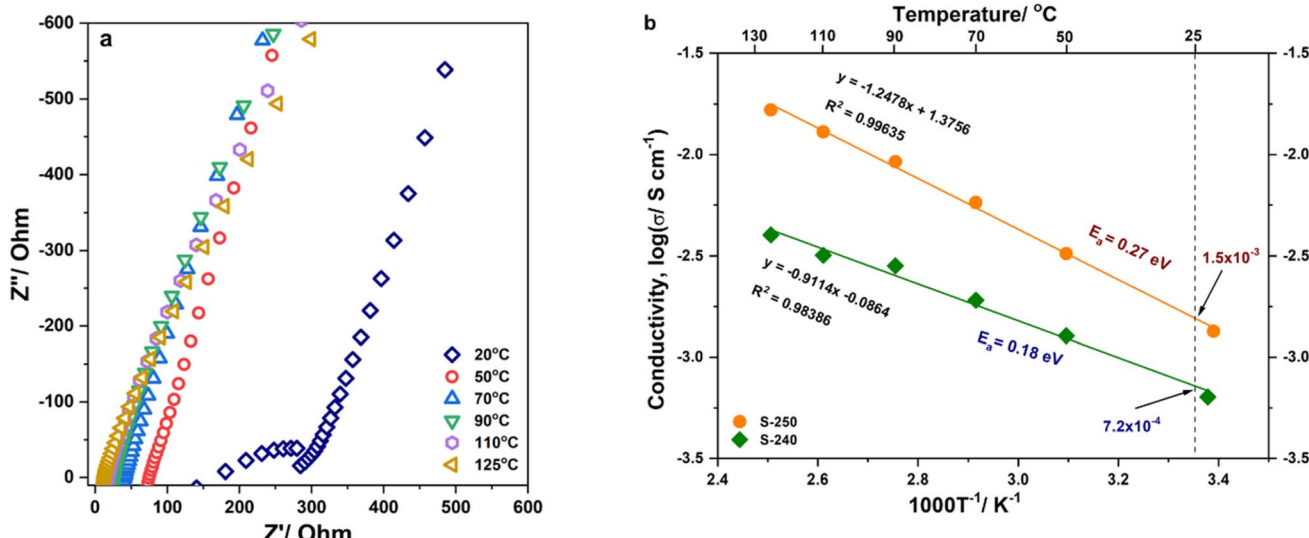


Fig. 5 (a) The impedance spectra of S-250 obtained at various temperatures from around room temperature (20 °C) to 125 °C; (b) temperature dependence of the ionic conductivity of S-240 and S-250.

suggests that amorphous $\text{Li}_4\text{P}_2\text{S}_7$ was partially decomposed during the heat treatment at 250 °C. These findings are consistent with the XRD and Raman results.

Fig. 5a shows the impedance spectra of S-250 over a frequency range of 10 Hz–10 MHz at temperatures ranging from 20 °C to 125 °C. At 20 °C, the spectrum displays a semi-circle and a low-frequency tail, which is consistent with the Li^+ blocking effect, indicating the ionic conductivity. The diameter of the semicircle decreases with increasing temperature and becomes almost negligible at 50 °C. The total impedance of the electrolyte pellet was determined from the intersection of the semicircle and the x-axis in the intermediate frequency region.³⁵ The temperature-dependent ionic conductivities of S-240 and S-250 were calculated from the total impedance values and are plotted in Fig. 5b. Notably, $\log_{10}\sigma$ exhibits an almost linear dependence on the inverse temperature, following the Arrhenius equation $\sigma = \sigma_0 \exp(-E_a/(k_B T))$. The ionic conductivities of S-240 and S-250 at 25 °C are 7.2×10^{-4} and $1.5 \times 10^{-3} \text{ S cm}^{-1}$, respectively. These values are comparable to the reported values of conductivities for $\text{Li}_7\text{P}_3\text{S}_{11}$ synthesized via liquid-phase methods using ACN and EA, which are higher than those obtained with 1,2-dimethoxyethane (Table 1).^{10,12,13} The calculated activation energies E_a for S-240 and S-250 are 0.18 and 0.27 eV,

respectively. Previous studies have reported that a higher crystalline fraction of $\text{Li}_7\text{P}_3\text{S}_{11}$ enhances ionic conductivity and reduces E_a ,³⁰ whereas the presence of $\text{Li}_4\text{P}_2\text{S}_6$ in $\text{Li}_7\text{P}_3\text{S}_{11}$ increases E_a .³⁶ The area fractions of amorphous $\text{Li}_4\text{P}_2\text{S}_7$, crystalline $\text{Li}_7\text{P}_3\text{S}_{11}$, $\text{Li}_4\text{P}_2\text{S}_6$, and $\beta\text{-Li}_3\text{PS}_4$ were calculated to evaluate the effect of $\text{Li}_4\text{P}_2\text{S}_6$ on the conductivity and activation energy of S-250 (Table 2). Therefore, the higher ionic conductivity of S-250 compared with S-240 is attributed to increased $\text{Li}_7\text{P}_3\text{S}_{11}$ crystallinity, while its higher E_a is attributed to the presence of $\text{Li}_4\text{P}_2\text{S}_6$.

Fig. 6a shows the variation of DC with time when a voltage of 0.5 V (DC) was applied to the S-250 sample. With nonblocking electrodes, a constant current was observed, whereas blocking electrodes initially exhibited polarization followed by a nearly constant current. The current with nonblocking electrodes was approximately four orders of magnitude higher than that with blocking electrodes, indicating that S-250 is a single-ion conductor with a lithium-ion transport number estimated to be higher than 0.999. Fig. 6b shows the cyclic voltammogram of S-250. The small inset shows an enlarged cyclic voltammetry curve in the range of 2.0–5.0 V vs. Li^+/Li . The cathodic current, corresponding to the Li reduction, started at approximately 0 V, confirming the stability of the prepared SE against Li metal. Except for the cathodic anodic peaks, no additional peaks were observed within the scanned range, indicating the compatibility of the S-250 with Li metal up to 5 V vs. Li^+/Li .

Fig. 7a shows SEM-EDS images of the prepared LIC@NMC111 and S-250 mixture, illustrating that the SE particles are well-distributed among NMC111 particles. To assess the compatibility of S-250 with high-voltage SSBs, NMC111 was employed as the active material to evaluate cycling performance at a constant current of 0.1C in the voltage range of 2.4–3.7 V vs. Li-In at room temperature (Fig. 7b). The charge-discharge capacities of the 1st cycle were 122 and 101 mAh $\text{g}_{\text{NMC}}^{-1}$. In the 10th cycle, the capacities were 138 and 137 mAh

Table 2 Area fraction of the NMR peaks for S-240 and S-250

Sample	Phase	Area (%)
S-240	$\text{Li}_4\text{P}_2\text{S}_7$ amorphous	49.6
	$\text{Li}_7\text{P}_3\text{S}_{11}$	21.8
	$\beta\text{-Li}_3\text{PS}_4$	28.6
S-250	$\text{Li}_4\text{P}_2\text{S}_7$ amorphous	13.5
	$\text{Li}_7\text{P}_3\text{S}_{11}$	69.4
	$\beta\text{-Li}_3\text{PS}_4$	5.5
	$\text{Li}_4\text{P}_2\text{S}_6$	11.6



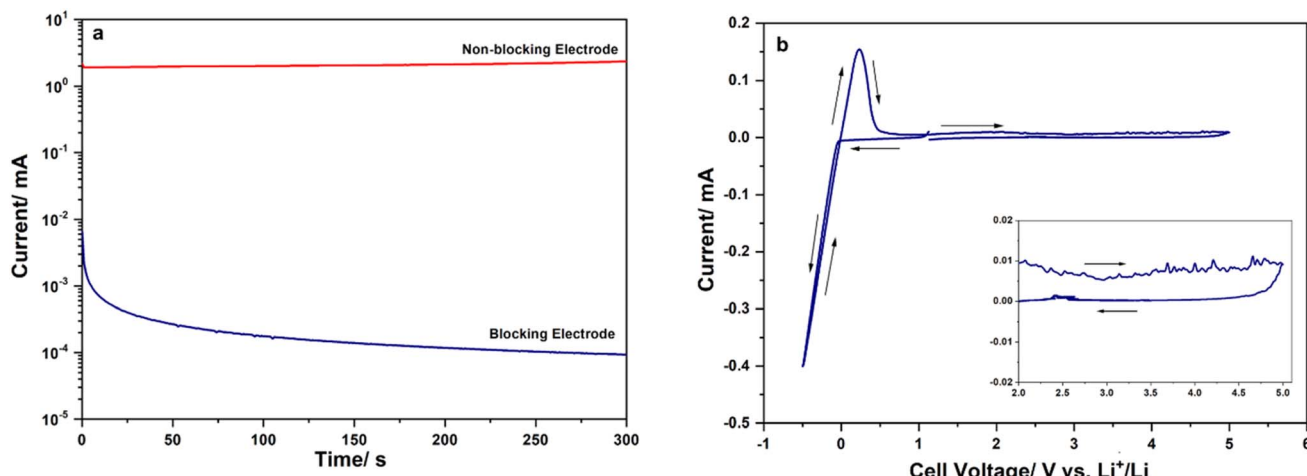


Fig. 6 (a) Change in DC with time when a voltage of 0.5 V (DC) was applied to the S-250 sample; (b) cyclic voltammogram of S-250 obtained at a scan rate of 5 mV s^{-1} between 0.5 and 5 V.

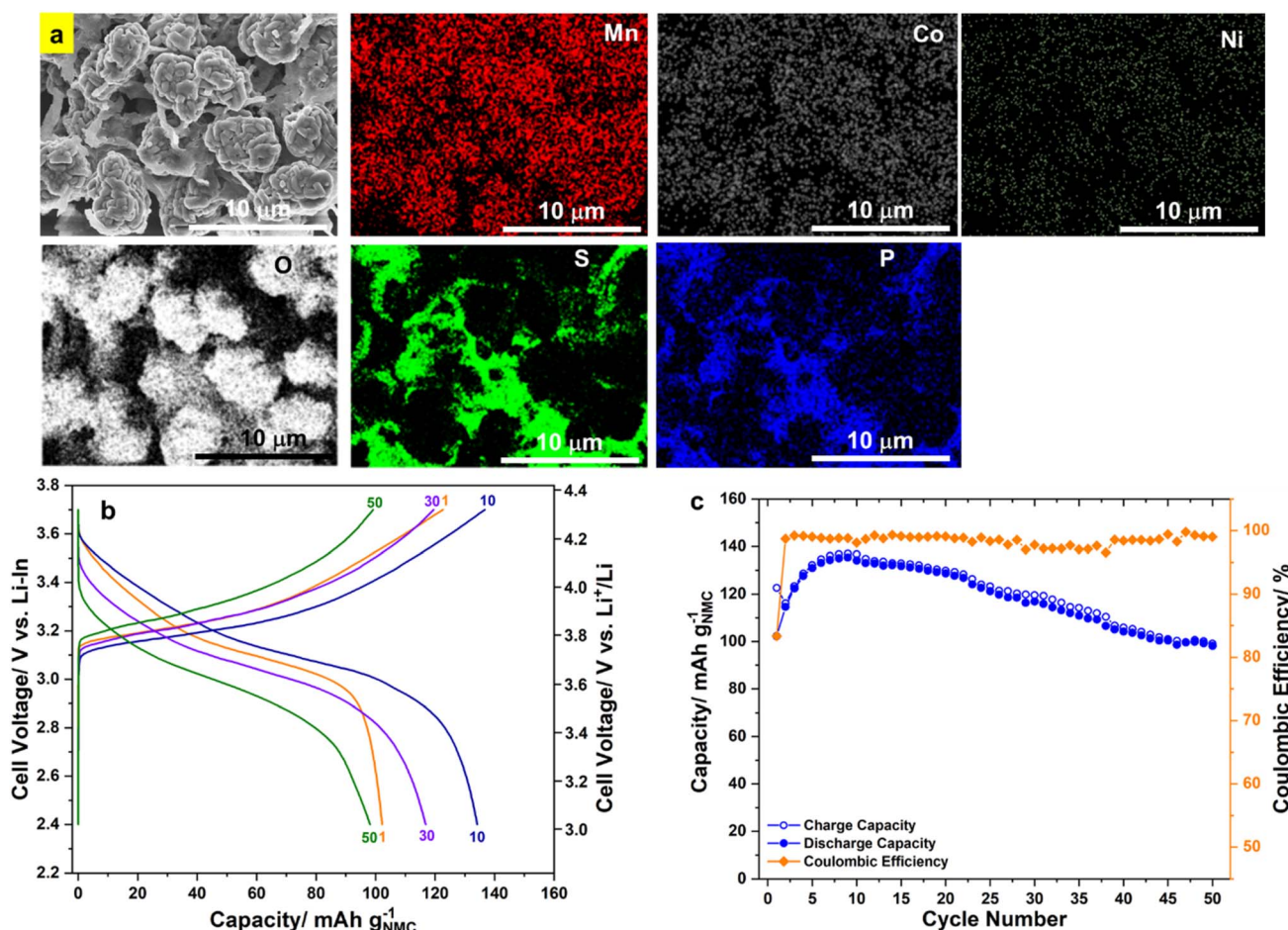


Fig. 7 (a) SEM-EDS images of the mixture of LIC@NMC11 and S-250; (b) 1st, 10th, 30th, and 50th charge–discharge curves of the prepared solid-state cell cycling at 0.1C between 3.7 and 2.4 V vs. Li–In; (c) charge–discharge capacities and CE of the prepared cell for 50 cycles.

$\text{g}_{\text{NMC}}^{-1}$, which were slightly higher than those of the 1st cycle. At the 30th cycle, the capacities were 120 and $119\text{ mAh g}_{\text{NMC}}^{-1}$, respectively. The initial coulombic efficiency (CE) was

approximately 83%. From 2nd cycle onwards, the CE was higher than 99%, indicating cell stability. Fig. 7c illustrates the charge–discharge capacities and CE of the prepared cell over 50 cycles,



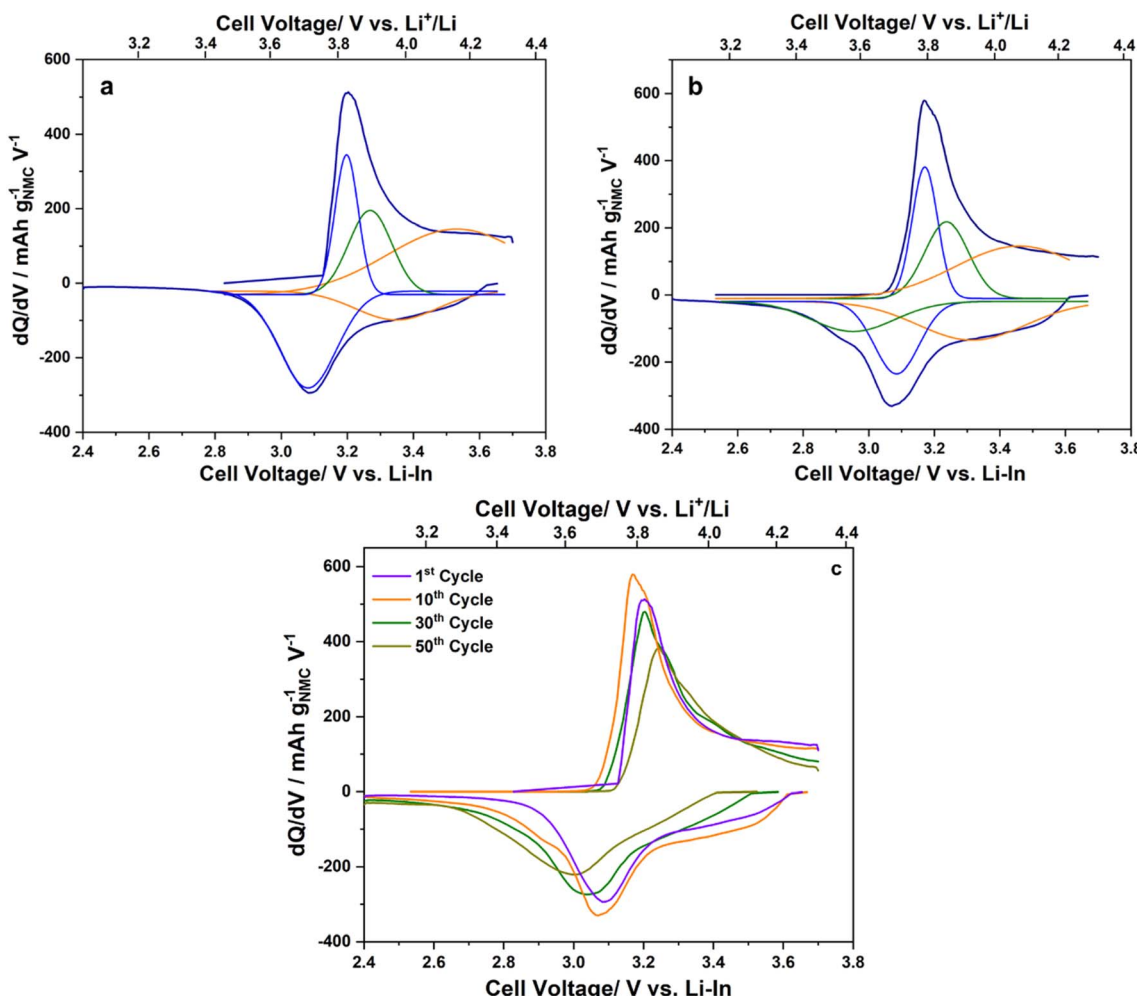


Fig. 8 dQ/dV curves of the NMC111 cathode at different cycles: (a) 1st, (b) 10th, (c) 1st, 10th, 30th, and 50th.

with the discharge capacity of the 50th-cycle nearly identical to that of the 1st cycle, further confirming the stability of the cell. These results demonstrate that the prepared S-250 SE is a promising candidate for SSBs.

Fig. 8 shows the differential capacity curves (dQ/dV) of the NMC111 cathode at different cycles to analyze the evolution of the voltage profile. In the 1st cycle (Fig. 8a), distinct redox peaks at 3.81/3.71 V vs. Li^+/Li were observed, attributed to $\text{Ni}^{3+}/\text{Ni}^{4+}$ oxidation/reduction associated with Li de-insertion/insertion.^{37,38} In the 10th cycle (Fig. 8b), these peaks shifted slightly to 3.80/3.70 V vs. Li^+/Li . Subsequently, the oxidation and reduction peaks shifted toward higher and lower voltage regions, respectively, indicating continuous capacity degradation (Fig. 8c). The redox peaks at 4.18/3.95 V vs. Li^+/Li in the 1st cycle are attributed to $\text{Co}^{4+}/\text{Co}^{3+}$ oxidation/reduction.^{37,38} These peaks shifted to the lower voltage region, which were again consistent with continuous capacity degradation. These results indicate that the electrode polarization increases with cycling. The redox peaks at about 3.84/3.55 V vs. Li^+/Li observed in the 10th cycle, which was gradually shifted to lower voltage region, is related to the oxidation/reduction of $\text{Ni}^{3+}/\text{Ni}^{2+}$.^{38,39} These peaks were not clearly visible in the 1st cycle, and their

appearance correlates with the increase in capacity from the 1st to the 10th cycle.

4. Conclusion

This study demonstrates that $\text{Li}_7\text{P}_3\text{S}_{11}$ SEs can be synthesized using EP to promote the reaction between Li_2S and P_2S_5 . The residue obtained after solvent removal at 190 °C is amorphous to XRD, but Raman spectroscopy confirms the presence of PS_4^{3-} and $\text{P}_2\text{S}_7^{4-}$ groups. Heating this residue at 230 °C, 240 °C, and 250 °C leads to the formation of $\text{Li}_7\text{P}_3\text{S}_{11}$ SE. ^{31}P NMR spectra results indicate that amorphous $\text{Li}_4\text{P}_2\text{S}_7$ reacts with $\beta\text{-Li}_3\text{PS}_4$ to yield $\text{Li}_7\text{P}_3\text{S}_{11}$. The prepared $\text{Li}_7\text{P}_3\text{S}_{11}$ SE exhibited an ionic conductivity of $1.5 \times 10^{-3} \text{ S cm}^{-1}$ at 25 °C with an activation energy of 0.27 eV. The electrochemical measurements show that the prepared SE is stable up to 5.0 V vs. Li^+/Li , demonstrating its suitability for SSB applications.

Author contributions

TAT: investigation, formal analysis, data curation, formal analysis, resources; NHHP: conceptualization, methodology,



writing – original draft, visualization, supervision, project administration, writing – review & editing.

Conflicts of interest

The authors declare that they have no known competing financial interests or personal relationships that could have appeared to influence the work reported in this paper.

Data availability

The data itself is presented in the form of figures and tables in this manuscript.

Supplementary information is available. See DOI: <https://doi.org/10.1039/d5ra05281e>.

Acknowledgements

We acknowledge Ho Chi Minh City University of Technology (HCMUT), VNU-HCM for supporting this study. The authors thank Rio Jefferson (Enago; <https://www.enago.com/vnuhcm/>) for the English language review.

References

- 1 R. Chen, W. Qu, X. Guo, L. Li and F. Wu, The pursuit of solid-state electrolytes for lithium batteries: from comprehensive insight to emerging horizons, *Mater. Horiz.*, 2016, **3**, 487–516.
- 2 S. Chen, K. Wen, J. Fan, Y. Bando and D. Golberg, Progress and future prospects of high-voltage and high-safety electrolytes in advanced lithium batteries: from liquid to solid electrolytes, *J. Mater. Chem. A*, 2018, **6**, 11631–11663.
- 3 C. Xu, L. Chen and F. Wu, Unveiling the power of sulfide solid electrolytes for next-generation all-solid-state lithium batteries, *Next Mater.*, 2025, **6**, 100428.
- 4 T. Yu, Y. Liu, H. Li, Y. Sun, S. Guo and H. Zhou, Ductile Inorganic Solid Electrolytes for All-Solid-State Lithium Batteries, *Chem. Rev.*, 2025, **125**, 3595–3662.
- 5 M. K. Tufail, N. Ahmad, L. Yang, L. Zhou, M. A. Naseer, R. Chen and W. Yang, A panoramic view of Li₂P₃S₁₁ solid electrolytes synthesis, structural aspects and practical challenges for all-solid-state lithium batteries, *Chin. J. Chem. Eng.*, 2021, **39**, 16–36.
- 6 Y. Seino, T. Ota, K. Takada, A. Hayashi and M. Tatsumisago, A sulphide lithium super ion conductor is superior to liquid ion conductors for use in rechargeable batteries, *Energy Environ. Sci.*, 2014, **7**, 627–631.
- 7 H. Gamo, A. Nagai and A. Matsuda, Toward Scalable Liquid-Phase Synthesis of Sulfide Solid Electrolytes for All-Solid-State Batteries, *Batteries*, 2023, **9**, 355–371.
- 8 M. Calpa, N. C. Rosero-Navarro, A. Miura and K. Tadanaga, Electrochemical performance of bulk-type all-solid-state batteries using small-sized Li₂P₃S₁₁ solid electrolyte prepared by liquid phase as the ionic conductor in the composite cathode, *Electrochim. Acta*, 2019, **296**, 473–480.
- 9 N. H. H. Phuc, H. Gamo, K. Hikima, H. Muto and A. Matsuda, Preparation of CaI₂-Doped Li₂P₃S₁₁ by Liquid-Phase Synthesis and Its Application in an All-Solid-State Battery with a Graphite Anode, *Energy Fuels*, 2022, **36**, 4577–4584.
- 10 R. C. Xu, X. H. Xia, Z. J. Yao, X. L. Wang, C. D. Gu and J. P. Tu, Preparation of Li₂P₃S₁₁ glass-ceramic electrolyte by dissolution-evaporation method for all-solid-state lithium ion batteries, *Electrochim. Acta*, 2016, **219**, 235–240.
- 11 Y. Wang, D. Lu, M. Bowden, P. Z. El Khoury, K. S. Han, Z. D. Deng, J. Xiao, J.-G. Zhang and J. Liu, Mechanism of Formation of Li₂P₃S₁₁ Solid Electrolytes through Liquid Phase Synthesis, *Chem. Mater.*, 2018, **30**, 990–997.
- 12 J. Zhou, Y. Chen, Z. Yu, M. Bowden, Q. R. S. Miller, P. Chen, H. T. Schaeff, K. T. Mueller, D. Lu, J. Xiao, J. Liu, W. Wang and X. Zhang, Wet-chemical synthesis of Li₂P₃S₁₁ with tailored particle size for solid state electrolytes, *Chem. Eng. J.*, 2022, **429**, 132334.
- 13 S. Ito, M. Nakakita, Y. Aihara, T. Uehara and N. Machida, A synthesis of crystalline Li₂P₃S₁₁ solid electrolyte from 1,2-dimethoxyethane solvent, *J. Power Sources*, 2014, **271**, 342–345.
- 14 H. Gamo, A. Nagai and A. Matsuda, The effect of solvent on reactivity of the Li₂S-P₂S₅ system in liquid-phase synthesis of Li₂P₃S₁₁ solid electrolyte, *Sci. Rep.*, 2021, **11**, 21097.
- 15 N. H. H. Phuc, K. Morikawa, T. Mitsuhiro, H. Muto and A. Matsuda, Synthesis of plate-like Li₃PS₄ solid electrolyte via liquid-phase shaking for all-solid-state lithium batteries, *Ionics*, 2017, **23**, 2061–2067.
- 16 T. Yamamoto, N. H. H. Phuc, H. Muto and A. Matsuda, Preparation of Li₂P₂S₈I Solid Electrolyte and Its Application in All-Solid-State Lithium-Ion Batteries with Graphite Anode, *Electron. Mater. Lett.*, 2019, **15**, 409–414.
- 17 N. H. H. Phuc, T. Maeda, T. Yamamoto, H. Muto and A. Matsuda, Preparation of Li₃PS₄-Li₃PO₄ Solid Electrolytes by Liquid-Phase Shaking for All-Solid-State Batteries, *Electron. Mater.*, 2021, **2**, 39–48.
- 18 N. H. H. Phuc, T. Yamamoto, H. Muto and A. Matsuda, Fast synthesis of Li₂S-P₂S₅-LiI solid electrolyte precursors, *Inorg. Chem. Front.*, 2017, **4**, 1660–1664.
- 19 C. Liu, C. Miao, M. He, J. Wang, Q. Chen, S. Nie and W. Xiao, Optimized layered ternary LiNi_{0.5}Co_{0.2}Mn_{0.3}O₂ cathode materials modified with ultrathin Li₃InCl₆ fast ion conductor layer for lithium-ion batteries, *J. Power Sources*, 2023, **566**, 232961.
- 20 N. A. Khoa, N. T. M. Nguyet, T. V. Toan, L. M. Dang, N. X. Manh, T. A. Tu and N. H. H. Phuc, Synthesis of a Li_{3-x}InCl_{6-x} solid electrolyte and its application in all-solid-state batteries, *Solid State Ionics*, 2025, **421**, 116792.
- 21 B. Shao, R. Das, Y. Huang, R. Deng, S. Seelman and F. Han, Structural evolution during solution-based synthesis of Li₂P₃S₁₁ solid electrolyte by synchrotron X-ray total scattering, *J. Mater. Chem. A*, 2023, **11**, 17035–17044.
- 22 S. Ujiie, A. Hayashi and M. Tatsumisago, Preparation and ionic conductivity of (100-x)(0.8Li₂S·0.2P₂S₅)·xLiI glass-ceramic electrolytes, *J. Solid State Electrochem.*, 2012, **17**, 675–680.



- 23 B. Fan, Q. Zhang, Z. Luo, X. Zhang, H. Ma, P. Fan and B. Xue, Influence of precipitate/supernatant ratio during liquid-phase synthesis of solid electrolyte $\text{Li}_7\text{P}_3\text{S}_{11}$, *Solid State Ionics*, 2019, **343**, 115073.
- 24 A. Hayashi, T. Ohtomo, F. Mizuno, K. Tadanaga and M. Tatsumisago, All-solid-state Li/S batteries with highly conductive glass-ceramic electrolytes, *Electrochem. Commun.*, 2003, **5**, 701–705.
- 25 H. Nagata and J. Akimoto, Ionic Conductivity of Low-Crystalline $\text{Li}_4\text{P}_2\text{S}_6$ and $\text{Li}_4\text{P}_2\text{S}_6\text{-LiX}$ (X=Cl, Br, and I) Systems and Their Role in Improved Positive Electrode Performance in All-Solid-State LiS Battery, *ChemistrySelect*, 2020, **5**, 9926–9931.
- 26 C. Dietrich, D. A. Weber, S. J. Sedlmaier, S. Indris, S. P. Culver, D. Walter, J. Janek and W. G. Zeier, Lithium ion conductivity in $\text{Li}_2\text{S-P}_2\text{S}_5$ glasses – building units and local structure evolution during the crystallization of superionic conductors Li_3PS_4 , $\text{Li}_7\text{P}_3\text{S}_{11}$ and $\text{Li}_4\text{P}_2\text{S}_7$, *J. Mater. Chem. A*, 2017, **5**, 18111–18119.
- 27 R.-c. Xu, X.-h. Xia, X.-l. Wang, Y. Xia and J.-p. Tu, Tailored $\text{Li}_2\text{S-P}_2\text{S}_5$ glass-ceramic electrolyte by MoS_2 doping, possessing high ionic conductivity for all-solid-state lithium-sulfur batteries, *J. Mater. Chem. A*, 2017, **5**, 2829–2834.
- 28 A. Hayashi, K. Minami, S. Ujiie and M. Tatsumisago, Preparation and ionic conductivity of $\text{Li}_7\text{P}_3\text{S}_{11-z}$ glass-ceramic electrolytes, *J. Non-Cryst. Solids*, 2010, **356**, 2670–2673.
- 29 M. Murakami, K. Shimoda, S. Shiotani, A. Mitsui, K. Ohara, Y. Onodera, H. Arai, Y. Uchimoto and Z. Ogumi, Dynamical Origin of Ionic Conductivity for $\text{Li}_7\text{P}_3\text{S}_{11}$ Metastable Crystal As Studied by $6/7\text{Li}$ and 31P Solid-State NMR, *J. Phys. Chem. C*, 2015, **119**, 24248–24254.
- 30 Y. Seino, M. Nakagawa, M. Senga, H. Higuchi, K. Takada and T. Sasaki, Analysis of the structure and degree of crystallisation of $70\text{Li}_2\text{S-30P}_2\text{S}_5$ glass ceramic, *J. Mater. Chem. A*, 2015, **3**, 2756–2761.
- 31 R. Poirier, T. Robinson, D. Gajan, A. Lesage, M. Corral Valero, L. Lemaitre, D. Pasquier, A. Lambert, D. Uzio and C. Garneron, Unveiling Insights in the Formation Mechanism of $\text{Li}_3\text{PS}_4\cdot2\text{THF}$ Solvato-Complex: H_2S Release and Solvent-Phase Interaction, *Inorg. Chem.*, 2025, **64**, 7534–7542.
- 32 Z. Z. Hellmut Eckert and J. H. Kennedy, Structural Transformation of Non-Oxide Chalcogenide Glasses. The Short-Range Order of $\text{Li}_2\text{S-P}_2\text{S}_5$ Glasses Studied by Quantitative 31P and $6, 7\text{Li}$ High-Resolution Solid-state NMR, *Chem. Mater.*, 2010, **2**, 273–279.
- 33 C. Dietrich, M. Sadowski, S. Sicolo, D. A. Weber, S. J. Sedlmaier, K. S. Weldert, S. Indris, K. Albe, J. Janek and W. G. Zeier, Local Structural Investigations, Defect Formation, and Ionic Conductivity of the Lithium Ionic Conductor $\text{Li}_4\text{P}_2\text{S}_6$, *Chem. Mater.*, 2016, **28**, 8764–8773.
- 34 C. Dietrich, D. A. Weber, S. Culver, A. Senyshyn, S. J. Sedlmaier, S. Indris, J. Janek and W. G. Zeier, Synthesis, Structural Characterization, and Lithium Ion Conductivity of the Lithium Thiophosphate $\text{Li}_2\text{P}_2\text{S}_6$, *Inorg. Chem.*, 2017, **56**, 6681–6687.
- 35 K. Suzuki, M. Sakuma, S. Hori, T. Nakazawa, M. Nagao, M. Yonemura, M. Hirayama and R. Kanno, Synthesis, structure, and electrochemical properties of crystalline Li-P-S-O solid electrolytes: Novel lithium-conducting oxysulfides of $\text{Li}_{10}\text{GeP}_2\text{S}_{12}$ family, *Solid State Ionics*, 2016, **288**, 229–234.
- 36 K. Minami, A. Hayashi and M. Tatsumisago, Preparation and characterization of superionic conducting $\text{Li}_7\text{P}_3\text{S}_{11}$ crystal from glassy liquids, *J. Ceram. Soc. Jpn.*, 2010, **118**, 305–308.
- 37 Y. Shin, W. Choi, Y. Hong, S. Yoon, K. Ryu and S. Chang, Investigation on the microscopic features of layered oxide $\text{Li}[\text{Ni}_{1/3}\text{Co}_{1/3}\text{Mn}_{1/3}]_{\text{O}_2}$ and their influences on the cathode properties, *Solid State Ionics*, 2006, **177**, 515–521.
- 38 N. Yabuuchi, Y. Makimura and T. Ohzuku, Solid-State Chemistry and Electrochemistry of $\text{LiCo}_{1/3}\text{Ni}_{1/3}\text{Mn}_{1/3}\text{O}_2$ for Advanced Lithium-Ion Batteries: III. Rechargeable Capacity and Cycleability, *J. Electrochem. Soc.*, 2007, **154**, A314.
- 39 J. R. Croy, K. G. Gallagher, M. Balasubramanian, Z. Chen, Y. Ren, D. Kim, S.-H. Kang, D. W. Dees and M. M. Thackeray, Examining Hysteresis in Composite $x\text{Li}_2\text{MnO}_3\cdot(1-x)\text{LiMO}_2$ Cathode Structures, *J. Phys. Chem. C*, 2013, **117**, 6525–6536.

